Journal of Sound and Vibration (2002) **256**(5), 821–833
doi:10.1006/jsvi.5021, available online at http://www.idealibrary.com on IDEAL®

STUDY OF SOUND PROPAGATION OVER RANGE-DEPENDENT AND TOPOGRAPHIC GROUND BY FINITE DIFFERENCE MODEL

H. DONG

Seismics and Formation Physics, Sintef Petroleum Research, 7465 Trondheim, Norway.
E-mail: hefeng.dong@iku.sintef.no

C. MADSHUS AND A. M. KAYNIA

Norwegian Geotechnical Institute, Oslo, Norway

J. M. HOVEM

Department of Telecommunications/Acoustics, Norwegian University of Science and Technology, Trondheim, Norway

AND

L. R. HOLE

Norwegian Institute for Air Research, Kjeller, Norway

(*Received* 12 *October* 2001, *and in final form* 13 *November* 2001)

This paper extends an earlier study on sound propagation over poro-elastic layered ground to range-dependent and topographic ground. The model is based on a pressure–velocity finite-difference formulation and is coded in the computer program PORAC. To highlight the influence of range-dependent parameters and topographic features on sound propagation, four cases are considered: (i) a homogeneous poro-elastic half-space (the base case); (ii) the base case with a zone in the ground with a higher permeability; (iii) the base case with a zone of higher stiffness; (iv) the base case with a rectangular hill. The paper presents typical results of sound propagation in these cases comprising synthetic time histories of overpressure in the atmosphere and ground vibration as well as snapshots of the response of the atmosphere–ground system at selected times. Comparative results in these cases serve to highlight the effect of the various non-homogeneities considered in this study.

1. INTRODUCTION

In recent years, researchers have used different approaches to study the propagation of airborne acoustic pulses. The applied methods have included complex impedance ground representation (e.g., reference [1]), rigid-porous approximation (references [2, 3]), visco-elastic approach (e.g., reference [4]), and frequency-wavenumber FFP (e.g., Schmidt, [5]). The former model has been used by Chotiros [6] for studying sound propagation in water-saturated sand in the 10–100 kHz frequency band and by Hole *et al.* [7] for the simulation of low-frequency impulse noise and ground vibration in the Norwegian airblast tests in Haslemoen. A similar model has been used by Tooms *et al.* [8] to predict sound

0022-460X/02/$35.00

propagation at single frequencies and the possible effect of ground elasticity on atmospheric sound propagation.

A different computational technique based on pressure–velocity finite-difference formulation (PV–FD) was developed by Dong *et al.* [9] and used to simulate the propagation of sound over a layered poro-elastic ground. This model is formulated in an axisymmetric co-ordinate system and is a modification of the model originally developed for simulating acoustic wave propagation in borehole logging and seismics [10]. This paper extends the finite-difference computational technique of Dong *et al.* [9] to range-dependent and topographic ground conditions. Four cases are considered: (i) a homogeneous poro-elastic half-space (the base case, Case A); (ii) the base case with a zone in the ground with a higher permeability (Case B); (iii) the base case with a zone of higher stiffness (Case C); (iv) the base case with a rectangular hill (Case D). The paper presents typical results of sound propagation in these cases comprising synthetic time histories of overpressure in the atmosphere and ground vibration as well as snapshots of the response of the atmosphere–ground system at selected times. Comparative results in these cases serve to highlight the effect on the various non-homogeneities considered in this study.

2. THEORY AND METHOD

Figure 1 sketches the type of problems considered in this study. The model consists of a homogeneous atmospheric half-space above a poro-elastic ground with arbitrary terrain condition and range-dependent properties. The ground is assumed to satisfy Biot's theory [11, 12]. A cylindrical co-ordinate system (r, θ, z) is considered and a point source is located on the z-axis above the ground. Under azimuth symmetry (i.e., wave field being independent of θ) the air pressure $P(r, z, t)$ and the velocities for a heterogeneous poro-elastic ground, $\mathbf{u}(r, z, t)$ and $\mathbf{W}_\phi(r, z, t)$, satisfy the equations [9]:

$$\partial_{tt} P(r,z,t)/(\rho_0 V_0^2) = \nabla\cdot(\nabla P(r,z,t)/\rho_0) + 2g(t)\delta(r)\delta(z-z_0)/r, \quad 0 \leqslant r < +\infty,$$
$$h < z < +\infty, t > 0, \tag{1}$$

$$\rho_1\partial_{tt}\mathbf{u} + e\rho_1\partial_{tt}\mathbf{W}_\phi + b\partial_t\mathbf{W}_\phi = \mathbf{D}_1(\mathbf{u}; \alpha M\phi) + \mathbf{D}_1(\mathbf{W}_\phi; M\phi^2),$$
$$\rho\partial_{tt}\mathbf{u} + \rho_1\partial_{tt}\mathbf{W}_\phi = \mathbf{D}_1(\mathbf{u}; K_b - 2\mu_b/3 + \alpha^2 M) + \mathbf{D}_1(\mathbf{W}_\phi; \alpha M\phi) + \mathbf{D}_2(\mathbf{u};\mu_b),$$
$$0 \leqslant r < +\infty, -\infty < z < h, t > 0, \tag{2}$$

where $\delta(\mathbf{r})$ is the Kronecker Delta, $g(t)$ defines the time variation of the point source, (r_0, z_0) specifies the position of the point source, and V_0 and ρ_0 are the sound speed and mass density of the atmosphere. The vector $\mathbf{u}$ denotes the velocity of the solid frame, $\mathbf{W} = \phi\cdot(\mathbf{U} - \mathbf{u})$ is the velocity of the pore fluid relative to the solid frame in the ground, $\mathbf{W}_\phi = \mathbf{W}(r, z, t)/\phi$, $\mathbf{U}$ represents the velocity vector of the pore fluid, ϕ is porosity and e is tortuosity. The poro-elastic mass parameters are identified by $\rho_1 = \phi\rho_f$ and $\rho = \phi\rho_f + (1-\phi)\rho_s$ whereρ_s and ρ_f are the mass densities of the solid grains and the pore fluid respectively. The energy dissipation in the porous medium is reflected by the parameter $b = \phi^2\eta/\kappa$, where κ denotes the permeability and η is the dynamic viscosity of the pore fluid. The stiffness attribute of the porous medium is represented by the shear modulus of the solid frame μ_b, $\alpha = 1 - K_b/K_s$ and $M = (\phi/K_f + (\alpha - \phi)/K_s)^{-1}$, where K_b, K_s and K_f are the bulk moduli of the solid frame, solid grains and the pore fluid respectively. Finally, the differential operators $\mathbf{D}_1$ and $\mathbf{D}_2$ are defined by

$$\mathbf{D}_1(\mathbf{f}; A) = A\nabla\nabla\cdot\mathbf{f} + \nabla A\nabla\cdot\mathbf{f}, \tag{3}$$

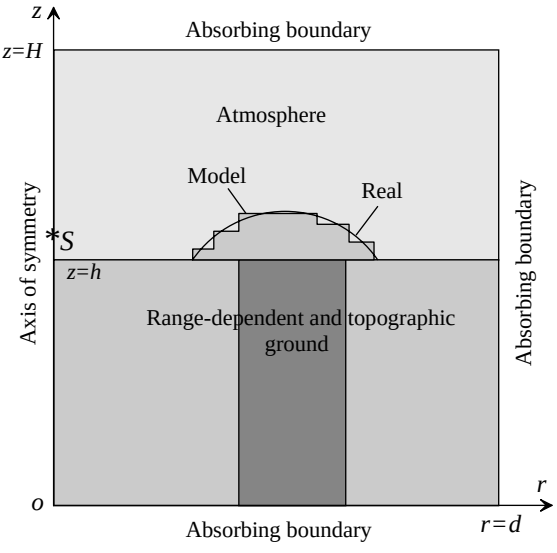

Figure 1. Model geometry used for the finite-difference simulation. A point source is located at z-axis above the ground with range-dependent and topographic characteristics.

$$\mathbf{D}_2(\mathbf{f}; B) = B\nabla\nabla\cdot\mathbf{f} + B\nabla^2\mathbf{f} + \nabla B\times(\nabla\times\mathbf{f}) + 2(\nabla B\cdot\nabla)\mathbf{f}. \tag{4}$$

If the ground is homogeneous, the wave equations for heterogeneous media reduce to

$$\left.\begin{aligned}&\rho_f\partial_{tt}\mathbf{u} + \rho_c\partial_{tt}\mathbf{W} + \frac{\eta}{\kappa}\partial_t\mathbf{W} = \alpha M\nabla(\nabla\cdot\mathbf{u}) + M\nabla(\nabla\cdot\mathbf{W})\\ &\rho\partial_{tt}\mathbf{u} + \rho_f\partial_{tt}\mathbf{W} = (H-\mu_b)\nabla(\nabla\cdot\mathbf{u}) + \mu_b\nabla^2\mathbf{u} + \alpha M\nabla(\nabla\cdot\mathbf{W})\end{aligned}\right\}, \tag{5}$$

where $\rho_c = e\rho_f/\phi$ and $H = K_b + 4/3\ \mu_b + \alpha^2 M$.

On the interfaces between atmosphere and poro-elastic medium, the continuity and equilibrium conditions result in

$$\left.\begin{aligned}&-\frac{1}{\rho_f}\partial_z P = \partial_t u_z + \partial_t W_z\\ &-\partial_t P = \alpha M\nabla\cdot\mathbf{u} + M\nabla\cdot\mathbf{W}\\ &-\partial_t P = H\nabla\cdot\mathbf{u} + \alpha M\nabla\cdot\mathbf{W} + 2\mu_b(\partial_z u_z - \nabla\cdot\mathbf{u})\\ &0 = \mu(\partial_z u_r + \partial_r u_z)\end{aligned}\right\} \quad (z = \text{constant}) \tag{6}$$

for horizontal interfaces and

$$\left.\begin{aligned}&-\frac{1}{\rho_f}\partial_r P = \partial_t u_r + \partial_t W_r\\ &-\partial_t P = \alpha M\nabla\cdot\mathbf{u} + M\nabla\cdot\mathbf{W}\\ &-\partial_t P = H\nabla\cdot\mathbf{u} + \alpha M\nabla\cdot W + 2\mu_b(\partial_r u_r - \nabla\cdot\mathbf{u})\\ &0 = \mu(\partial_z u_r + \partial_r u_z).\end{aligned}\right\} \quad (r = \text{constant}) \tag{7}$$

for vertical interfaces.

TABLE 1

Parameters of the ground

Group	ρ_f (kg/m^3)	K_f 10^6 Pa	ρ_s (kg/m^3)	K_s (10^6 Pa)	K_b (10^6 Pa)	μ_b (10^6 Pa)	κ (10^{-10} m^2)	ϕ
1	1·2	0·13	2700	9060	60·7	25·5	1·0	0·44
2	1·2	0·13	2700	9060	60·7	25·5	100·0	0·44
3	1·2	0·13	2700	11000	136·8	56·63	1·0	0·44
4	—	—	1500	—	62·6	29·4	0·0	0·0

To simulate the infinite lateral and vertical extent of the media, the far-end boundary as well as the top and bottom boundaries of the model is equipped with dashpots (denoted as absorbing boundary in Figure 1). This measure accounts for the radiation damping in the system. The numerical model, however, does not include the material damping resulting from inter-granular friction in the soil medium.

The governing equations satisfying the pertinent boundary conditions are solved by an integration technique and second order finite-difference formulation. The appendix gives a summary of the mathematical derivations. More details can be found in reference [9] where the validity of the implemented formulation is also illustrated through comparisons with the frequency-wavenumber solution of OASES [5] and full-scale measurements.

3. SIMULATIONS

3.1. CASES CONSIDERED

Four cases of ground conditions were considered in this study (see Figure 1). Case A is a homogeneous poro-elastic half-space with the parameters given under Group 1 in Table 1. Although the developed code can handle a layered ground and atmosphere, this option is not considered in this study. Case B is similar to Case A except that a region between $r = 100$ and 150 m in the ground was assigned a higher permeability ($\kappa_B = 100 \cdot \kappa_A$, Group 2 in Table 1). Case C is similar to Case A except that the seismic velocities V_p and V_s in the region $r = 100$–150 m was increased by 50% (Group 3 in Table 1). Finally, Case D defers from Case A by the addition of a rectangular hill of height 8·65 m on the ground in the range $r = 100$–150 m. The selection of a simple geometry for the hill was just a matter of convenience. Figure 1 shows how a realistic hill geometry could be represented by piecewise straight segments. The properties of the hill are listed under Group 4 in Table 1. The dynamic viscosity of the pore air and tortuosity in the four cases were taken as $\eta = 1{\cdot}74 \times 10^{-5}$ kg/m s and $e = 1{\cdot}25$.

The time function describing the acoustic source was taken as the first derivative of the Gaussian function:

$$g(t) = -2\xi(t - t_s)\,\mathrm{e}^{-[\xi(t-t_s)]^2} \tag{8}$$

with a Fourier transform which can be expressed as

$$G(\omega) = -\mathrm{i}\omega\sqrt{\pi/\xi}\,\mathrm{e}^{-(\omega^2/4\xi)+\mathrm{i}\omega t_s}, \tag{9}$$

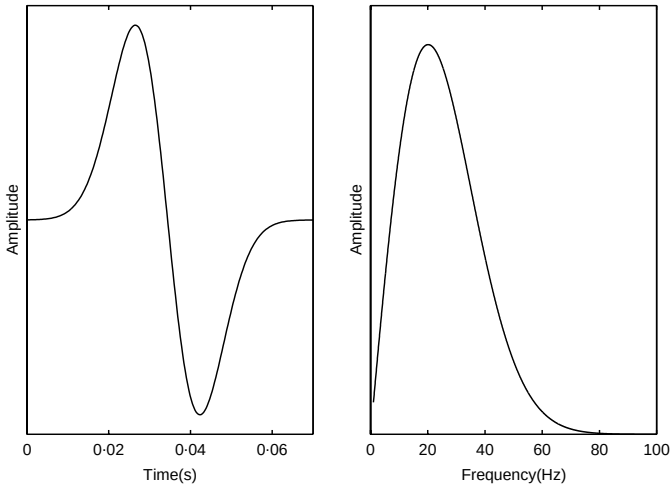

Figure 2. Source pulse and its Fourier amplitude spectrum used in present study. Central frequency is 20 Hz.

TABLE 2

Parameters of the source and atmosphere

f_0 (Hz)	f_{uh} (Hz)	ξ (s^{-2})	t_s (s)	ρ_0 (kg/m^3)	V_0 (m/s)
20	60	8000	0·035	1·2	330

where ξ and t_s are the pulse-width and time shift parameters respectively. The source and its Fourier spectrum are shown in Figure 2. The central frequency is 20 Hz.The source was positioned on the symmetry axis, 2 m above the ground. The parameters of the source and atmosphere are listed in Table 2.

3.2. NUMERICAL RESULTS

The finite-difference formulation presented in section 2 was used to simulate the dynamic overpressure in the air and the corresponding particle velocity in the ground for the four cases outlined in section 3.1.

Figure 3 displays the time histories of overpressure at 2 m above the ground, at distances of 80 and 160 m from the source. The results are plotted for Case A (homogeneous poro-elastic) as dashed line, Case B (poro-elastic with higher permeable zone) as dotted line and Case C (poro-elastic with stiffer zone) as solid line. As expected, the first arrivals at 80 m are identical in the three cases. At 160 m, however, both the amplitude and the dominant frequency for Case B reduce. This is due to the passage of the sound over the more permeable zone in Case B. The results further show that the stiffened zone in Case C does not change the amplitude nor the frequency content of the overpressure.

Figure 4 displays the corresponding time histories of the vertical particle velocity on the ground surface for the three cases considered in Figure 3. The arrival times as well as the amplitudes of the sound-induced wave and the surface (Rayleigh) wave are the same for the

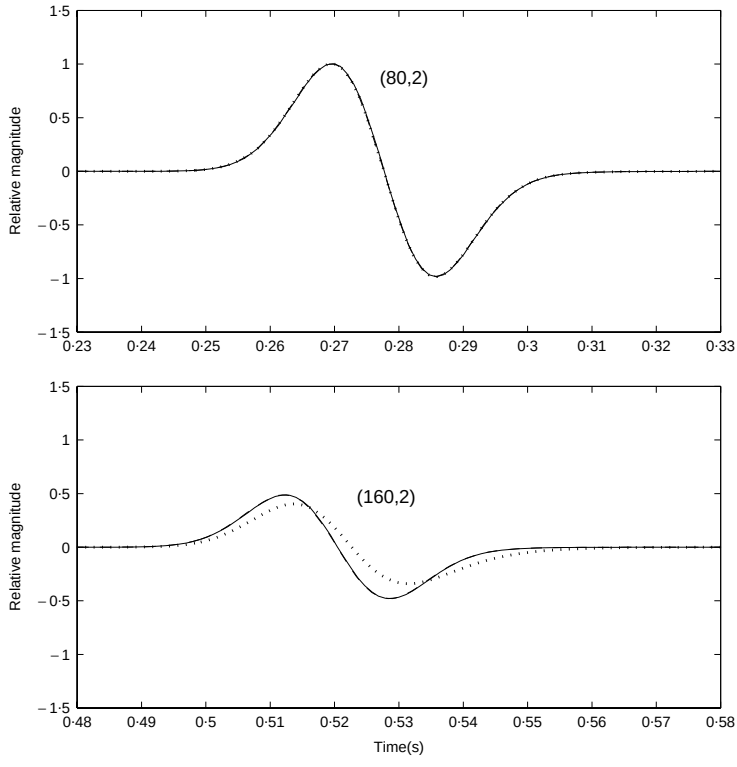

Figure 3. Comparison of air pressures among Case A (dashed line), Case B (dotted line) and Case C (solid line). Air pressure at 2 m above ground where the distances between source and receiver are 80 m (upper figure) and 160 m (lower figure) respectively.

velocity traces at 80 m. The trace for Case C, however, shows clearly the additional P-wave reflection from the stiffer zone. A very weak reflection can also be detected in Case B. For the particle ground velocity at 160 m, the amplitude of the first peak in Case C is different from the other two cases due to the near coincidence of the direct wave and P-wave. In addition, there is a second reflected P-wave from the stiff zone at about 0·7 s. The amplitude of the first peak in Case B is smaller than in Case A and a small reflected P-wave can be observed around 0·83 s. Finally, due to the stiffer zone in Case C, the surface wave has an earlier arrival (about 0·2 s) and smaller amplitude than in Cases A and B.

Figure 5 presents stacked plots with distance of the air overpressures at 2 m above ground (left set of figures) and the corresponding ground surface vibrations (right set of figures). The distances range from 16 to 176 with 8 m spacing. The upper two figures correspond to Case A, the middle figures to Case B and the bottom figures relate to Case C. For the pressure plots, the waveforms are almost identical in the three cases, except for a slight flattening of the signals in Case B due to the higher permeability zone in this case. For the velocity plots, the direct (blast-induced) and surface waves can be clearly discerned and the velocities of both waves calculated from the traces match well with the model parameters. Furthermore, both Cases B and C show clearly the influence of the added zones on the velocity signals which can be identified in the form of a reduced amplitude of the direct wave in Case B and a reduced amplitude and earlier arrival of the surface wave in Case C.

Figure 6 shows the same set of stacked plots for Case D (elastic hill). Since the overpressure plots are for 2 m above the ground, no traces are displayed in the range 100–150 m (the part of the shadow) due to the presence of the hill. The figure clearly shows

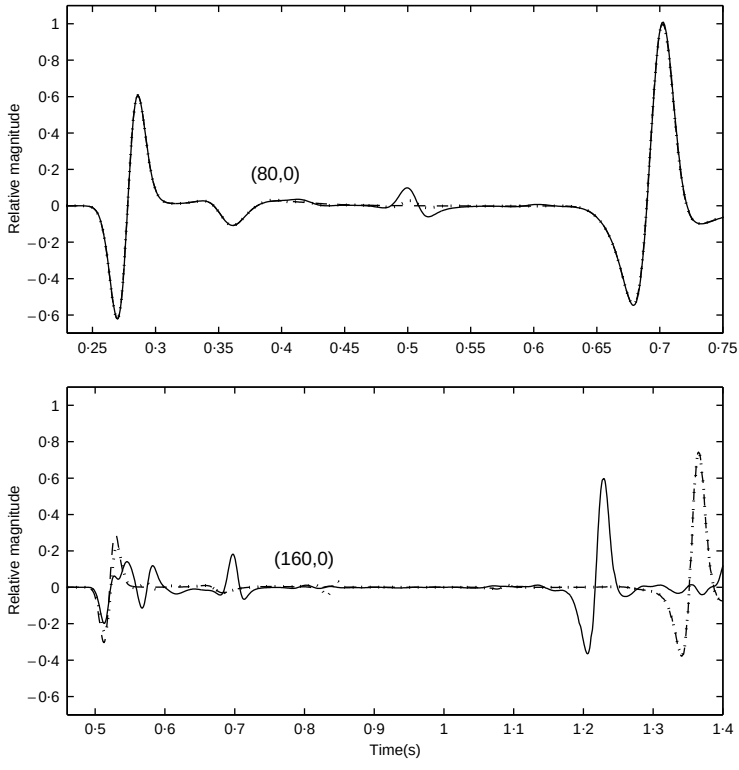

Figure 4. Comparison of vertical particle velocities on the ground surface in Case A (dashed line), Case B (dotted line) and Case C (solid line). Distances between source and receivers are 80 m (upper figure) and 160 m (lower figure).

the reflections from the hill in both the overpressure and ground motion traces. It is interesting further to note that the signals behind the hill become weaker because of partial reflection of the blast energy from the hill.

To examine the effect of the hill on the overpressure, Figure 7 presents comparisons between overpressures in Cases A and D at a height of 8·65 m (that is right at the hill top) at distances of 125 m (top plot) and 170 m (bottom plot). The considerably lower amplitude of the overpressure behind the hill signifies the noise isolation role of the hill.

A global picture of the sound propagation and its interaction with the ground can be observed by the snapshots of the spatial variation of air overpressure and particle velocity in the ground.

Figure 8 presents a set of such plots for Case A normalized by air overpressures at times 0·303, 0·453 and 0·543 s. The figures vividly display the P-, S- and Rayleigh-waves in the ground as well as the Mach surfaces associated with the two body waves. Because both the S- and P-wave velocities are lower than the sound speed in the atmosphere, the case considered here corresponds to a superseismic condition with two Mach surfaces moving with the propagating sound wave.

Figure 9 shows the same set of snap-shots for Case C. Location of the stiffer zone is marked in the plots. In addition to the general features observed in Figure 8, these plots show a remarkable reflection and refraction pattern in the ground waves by the stiff zone. It is also interesting to note in Figure 9(b) that the P-wave Mach surface vanishes over the stiffer zone as this zone represents a transeismic (and not a superseismic) case.

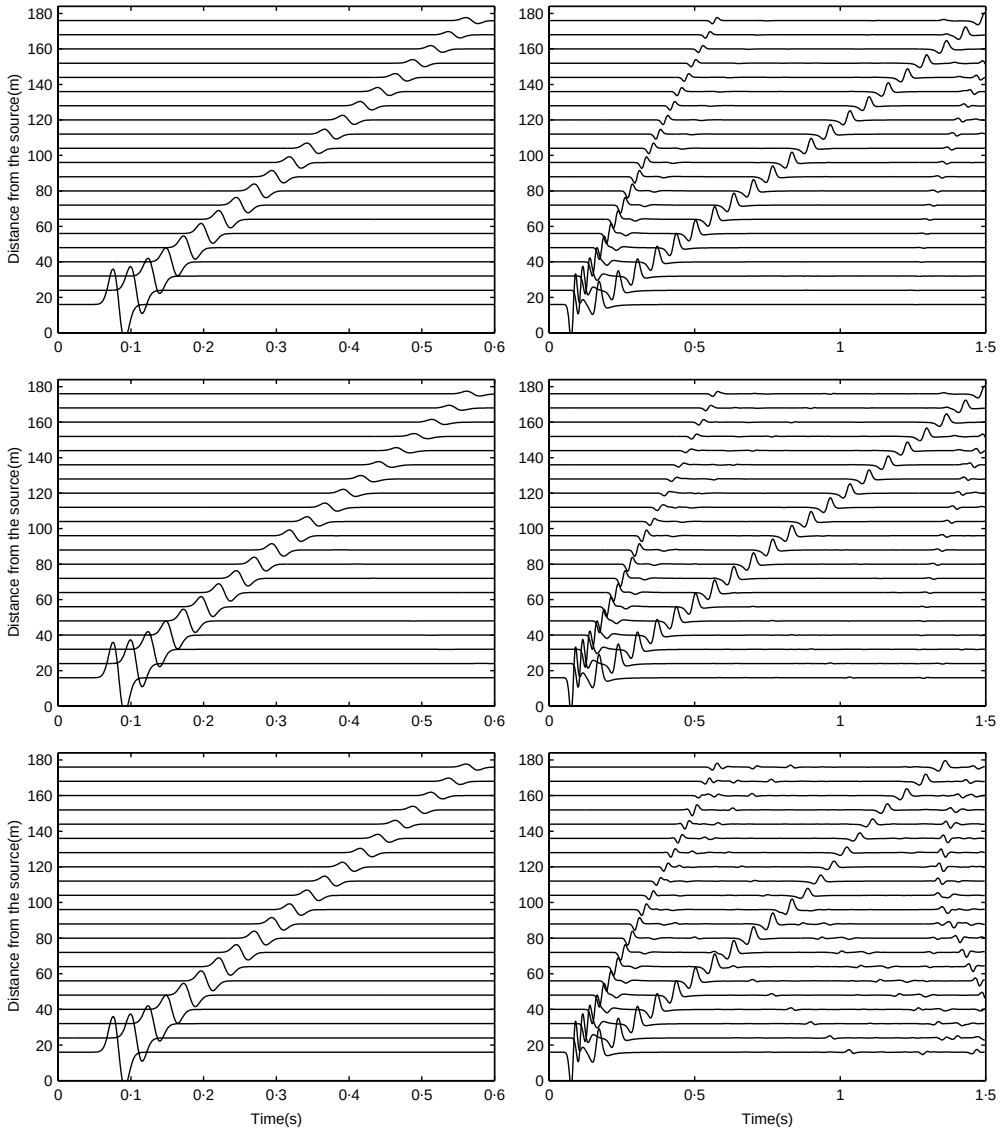

Figure 5. Stacked plots of air pressure at 2 m above ground (left figures) and vertical particle velocity on the ground surface (right figures) at distances from source ranging from 16 to 176 m with spacing of 8 m. Upper two figures corresponding to Case A, second two figures to Case B and lowest ones to Case C.

Figure 10 presents a similar set of snapshots for Case D. Large reflections from the hill can be clearly seen in these plots. In particular, there are two pairs of Mach surfaces, one connected to the incident body waves and the other related to the reflected body waves.

4. CONCLUSION

In this paper, the pressure–velocity finite-difference technique was used to simulate sound propagation over poro-elastic ground with range-dependent parameters and topographic

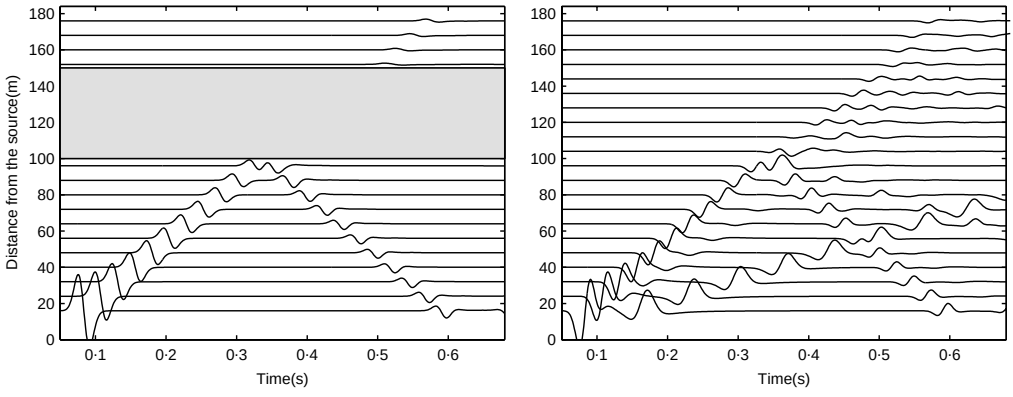

Figure 6. Stacked plots of air pressure for Case D at 2 m above ground (left) and vertical particle velocity on the ground surface (right) at different distances from the source ranging from 16 to 176 m with 8 m spacing.

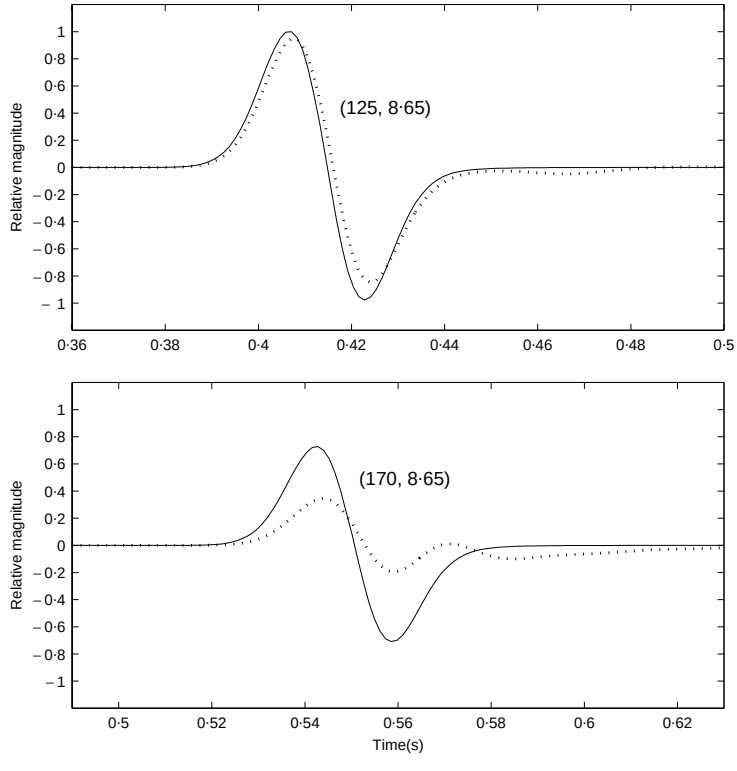

Figure 7. Comparisons of air pressures between Case A (solid line) and Case D (dotted line) at 8·65 m above ground with distances between the source and the receiver at 125 m (top) and 170 m (bottom) respectively.

features. Numerical simulations were carried out for different poro-elastic zone and hill. Typical results of the simulations of the overpressure in the atmosphere and the velocities of the ground were presented. The results for the range-dependent and topographic ground were compared with those in homogeneous ground. A number of snapshots of air overpressure and particle velocity in the ground were presented at different time steps to show the global wave propagation in these cases.

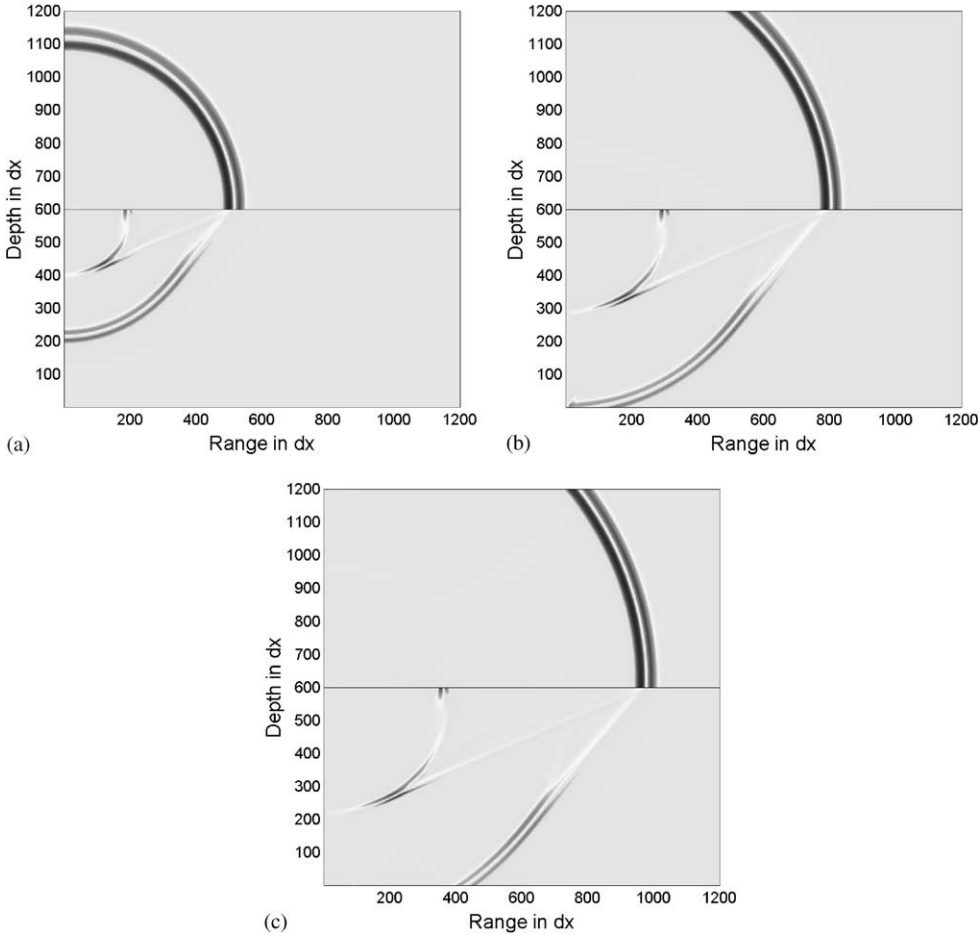

Figure 8. Snapshots of air pressure and vertical particle velocity in ground for Case A at $t = 0{\cdot}303$, $0{\cdot}453$ and $0{\cdot}543$ s.

ACKNOWLEDGMENTS

The authors wish to thank Prof. Ulf Kristiansen of the Norwegian University of Science and Technology for his helpful discussions and suggestions. Partial financial supports from Norwegian Defense Construction Service (NDCS) and the Norwegian Research Council under the program SIP-4 at Norwegian Geotechnical Institute (NGI) are gratefully acknowledged.

REFERENCES

1. F. G. DON and A. J. CRAMOND 1987 *Journal of the Acoustical Society of America* **81**, 1341–1349. Impulse propagation in a neutral atmosphere.
2. K. ATTENBOROUGH 1992 *Journal of Acoustical Society of America* **92**, 418–427. Ground parameter information for propagation modeling.
3. D. G. ALBERT and A. ORCUTT 1990 *Journal of the Acoustical Society of America* **87**, 93–100. Acoustic pulse propagation above grassland and snow: comparison of theoretical and experimental waveforms.

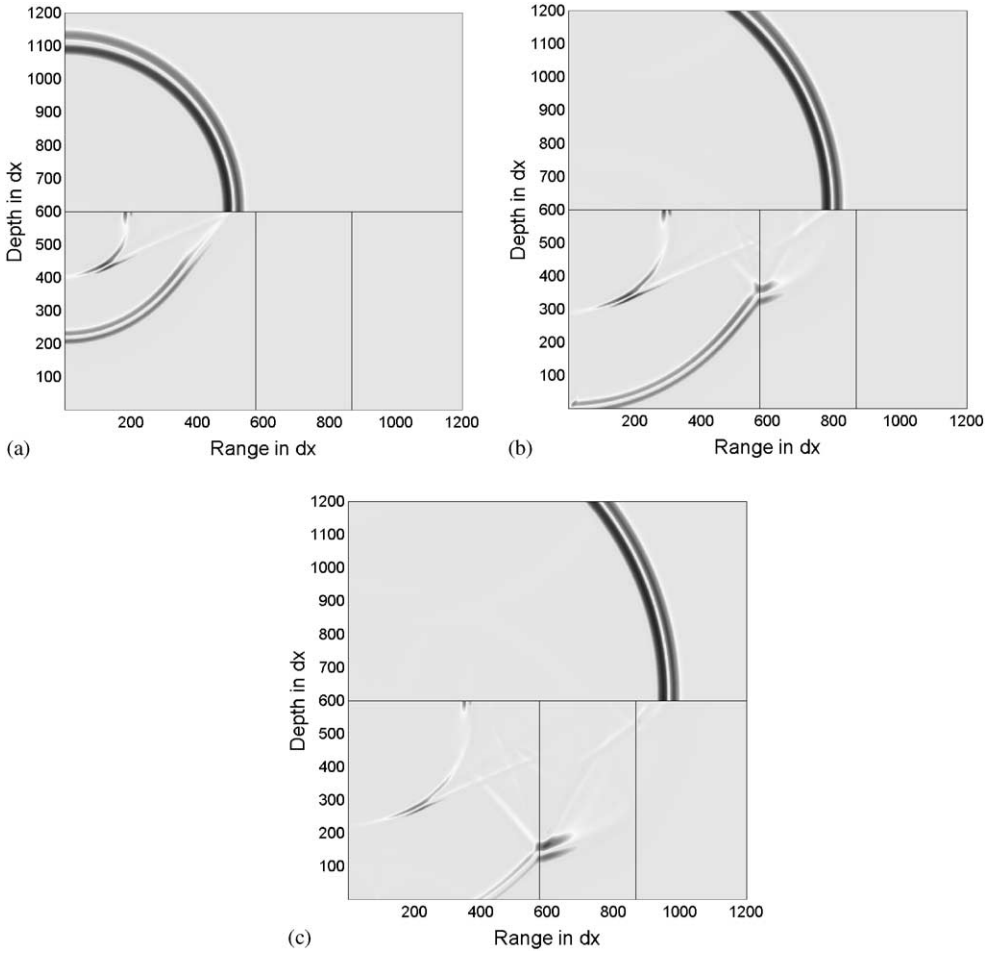

Figure 9. Snapshots of air pressure and vertical particle velocity in ground for Case C at $t = 0{\cdot}303$, $0{\cdot}453$ and $0{\cdot}543$ s.

4. L. R. HOLE 1997 *Applied Acoustics*. An experimental and theoretical study of propagation of acoustic pulses in a strongly refracting atmosphere.
5. H. SCHMIDT 1997 *OASES Version* 2.0, *Application and Upgrade Notes*. Department of Ocean Engineering, Massachusetts Institute of Technology.
6. N. P. CHOTIROS 1995 *Journal of the Acoustical Society of America* **97**, 199–214. Biot model of sound propagation in water-saturated sand.
7. L. R. HOLE, A. M. KAYNIA and C. MADSHUS 1998 *Journal of Sound and Vibration* **214**, 309–324. Measurement and simulation of low frequency impulse noise and ground vibration from airblasts.
8. S. TOOMS, S. TAHERIZADEH and K. ATTENBOROUGH 1993 *Journal of the Acoustical Society of America* **93**, 173–181. Sound propagation in a refracting fluid above a layered fluid-saturated porous elastic material.
9. H. DONG, A. M. KAYNIA, C. MADSHUS and J. M. HOVEM 2000 *Journal of Acoustical Society of America* **108**, 494–502. Sound propagation over layered poro-elastic ground by finite difference model.
10. H. DONG and K. WANG 1995 *Acta Geophysica Sinica* **38**(Supp. 1), 205–215.Finite-difference numerical simulation of elastic wave field in the elastic solid formation-fluid borehole.
11. M. A. BIOT 1956 *Journal of Acoustical Society of America* **28**, 168–178. I: low-frequency range. Theory of elastic waves in a fluid-saturated porous rock.

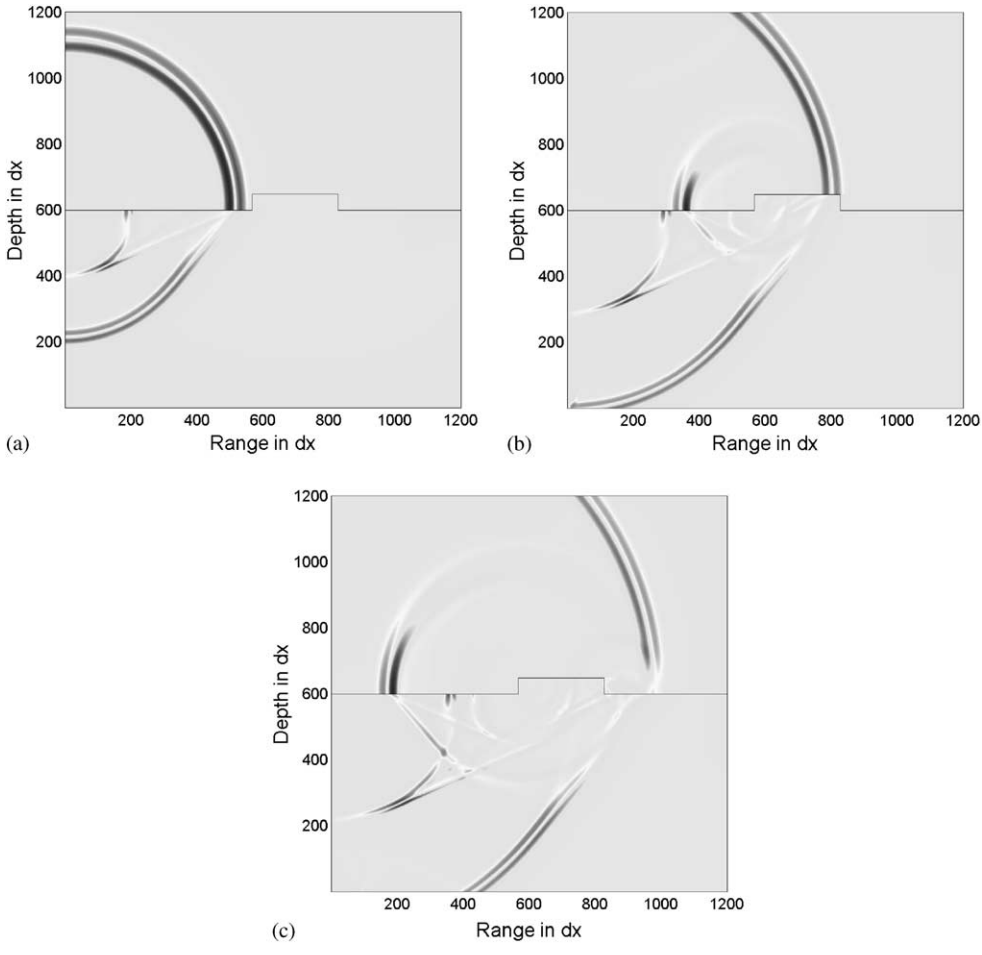

Figure 10. Snapshots of air pressure and vertical particle velocity in ground for Case D at $t = 0{\cdot}303$ s, $0{\cdot}453$ s and $0{\cdot}543$ s.

12. M. A. BIOT 1956 *Journal of Acoustical Society of America* **28**, 179–191. Theory of elastic waves in a fluid-saturated porous rock. II: high-frequency range.

APPENDIX A: FINITE DIFFERENCE FORMULATION

In inhomogeneous poro-elastic ground, the finite-difference solution of equation (2) can be simplified by using the finite-difference operators defined by the form

$$\Omega_j(\mathbf{f};\, A) = F_d \cdot \{\mathbf{D}_j(\mathbf{f};\, A)\}, \tag{A1}$$

where $j = 1, 2$ and $F_d \cdot \{\ \}$ indicates a finite-difference representation of the variable inside the brackets. By using this notation, equation (2) can be expressed as

$$\left\{\begin{aligned} &F_d\left\{\rho_1 \partial_{tt}\mathbf{u} + e\rho_1 \partial_{tt}\mathbf{W}_\phi + \phi^2 \frac{\eta}{\kappa}\partial_t \mathbf{W}_\phi\right\} = \overrightarrow{\Omega}_1(\mathbf{u};\, \alpha M\phi) + \overrightarrow{\Omega}_1(\mathbf{W}_\phi;\, M\phi^2) = \mathbf{\Phi}_1^k \\ &F_d\{\rho \partial_{tt}\mathbf{u} + \rho_1 \partial_{tt}\mathbf{W}_\phi\} = \overrightarrow{\Omega}_1(\mathbf{u};\, \lambda_b + \alpha^2 M) + \overrightarrow{\Omega}_1(\mathbf{W}_\phi;\, \alpha M\phi) + \overrightarrow{\Omega}_2(\mathbf{u};\, \mu_b) = \mathbf{\Phi}_2^k \end{aligned}\right\}, \tag{A2}$$

where $\mathbf{\Phi}_1^k$ and $\mathbf{\Phi}_2^k$ contain only spatial derivatives that need to be evaluated at the current time $k\Delta t$ in the context of a time marching algorithm. Using the standard second order explicit finite-difference approximations

$$\left\{\begin{aligned}\frac{\mathrm{d}u}{\mathrm{d}x} &\approx \frac{u(x+\Delta x)-u(x-\Delta x)}{2\Delta x}\\ \frac{d^2u}{dx^2} &\approx \frac{u(x+\Delta x)-2u(x)+u(x-\Delta x)}{\Delta x^2}\end{aligned}\right\}, \tag{A3}$$

one can derive the finite-difference schemes for $\mathbf{\Phi}_1^k$ and $\mathbf{\Phi}_2^k$. Using the central finite-difference representation in time on the left-hand side of equation (A3) and rearranging the terms, one can write

$$\left\{\begin{aligned}a_{11}\mathbf{u}^{k+1} + a_{12}\mathbf{W}_\phi^{k+1} &= \mathbf{b}_1 + (\Delta t)^2\mathbf{\Phi}_1^k\\ a_{21}\mathbf{u}^{k+1} + a_{22}\mathbf{W}_\phi^{k+1} &= \mathbf{b}_2 + (\Delta t)^2\mathbf{\Phi}_2^k\end{aligned}\right\}. \tag{A4}$$

The vectors $\mathbf{u}^{k+1}$and $\mathbf{W}^{k+1}$ can be obtained from

$$\mathbf{u}^{k+1} = \mathbf{\Delta}_1/\Delta, \qquad \mathbf{W}_\phi^{k+1} = \mathbf{\Delta}_2/\Delta, \tag{A5}$$

where a_{ij}, $\mathbf{b}_i$, $\mathbf{\Delta}_i$ $(i, j = 1, 2)$ and Δ are expressed as

$$\left\{\begin{aligned}a_{11} &= \rho_1, a_{12} = E\rho_1(1 + b\Delta t/(2E\rho_1))\\ a_{21} &= \rho, a_{22} = \rho_1\\ \mathbf{b}_1 &= \rho_1(2\mathbf{u}^k - \mathbf{u}^{k-1}) + E\rho_1[2\mathbf{W}_\phi^k - (1 - b\Delta t/(2E\rho_1))\mathbf{W}_\phi^{k-1}]\\ \mathbf{b}_2 &= \rho(2\mathbf{u}^k - \mathbf{u}^{k-1}) + \rho_1(2\mathbf{W}_\phi^k - \mathbf{W}_\phi^{k-1})\end{aligned}\right\}. \tag{A6}$$

$$\left\{\begin{aligned}\Delta_1 &= a_{22}[(\Delta t)^2\mathbf{\Phi}_1^k + \mathbf{b}_1] - a_{12}[(\Delta t)^2\mathbf{\Phi}_2^k + \mathbf{b}_2]\\ \Delta_2 &= a_{11}[(\Delta t)^2\mathbf{\Phi}_2^k + \mathbf{b}_2] - a_{21}[(\Delta t)^2\mathbf{\Phi}_1^k + \mathbf{b}_1]\\ \Delta &= a_{11}a_{22} - a_{12}a_{21}\end{aligned}\right\}. \tag{A7}$$

The velocity of the pore fluid at the next time step can be obtained from equation (A5) as

$$\mathbf{U}^{k+1} = \mathbf{u}^{k+1} + \mathbf{W}_\phi^{k+1} \tag{A8}$$